Journal of Alloys and Compounds 688 (2016) 260–269

Contents lists available at ScienceDirect

Journal of Alloys and Compounds

journal homepage: http://www.elsevier.com/locate/jalcom

Aqueous hydroxylation mediated synthesis of crystalline calcium uranate particles

Weixuan Ding [a, *], Johannes A. Botha [a], Bruce C. Hanson [a], Ian T. Burke [b]

[a] School of Chemical & Process Engineering, University of Leeds, Leeds LS2 9JT, UK
[b] School of Earth & Environment, University of Leeds, Leeds LS2 9JT, UK

ARTICLE INFO

Article history:
Received 19 May 2016
Received in revised form
13 July 2016
Accepted 14 July 2016
Available online 18 July 2016

Keywords:
Uranate
U(VI)
Synthesis
Precipitation
Particles
Crystallisation

ABSTRACT

Metal uranates(VI) are solubility limiting U(VI) phases under high pH conditions and may act as suitable long-term wasteforms. The precipitation and thermal phase development mechanisms of calcium uranate particles formed via aqueous hydroxylation reactions are studied in order to address the lack of aqueous synthesis methods currently available. Hydrous Ca-deficient uranate particles formed from aqueous solutions saturated in U(VI) oligomers were found to thermally decompose via several weight-loss steps between 100 and 800 °C. Crystalline calcium uranate ($Ca_2U_3O_{11}$) is initially formed at 700 °C via dehydration and dehydroxylation-olation reactions under redox-neutral conditions. This initial phase decomposes to biphasic $CaUO_4$-UO_2 particles at 800 °C via a reductive pathway.

1. Introduction

Global legacy civil and military nuclear activities have accumulated ~1200 kt [1] of depleted uranium (dU at ~0.3% U-235). The low market cost of natural uranium and a lack in fast reactor technology until at least 2030 [2] reduces the economic case for using dU in civil power generation. Whilst down-blending of highly enriched U stocks (1.44 kt, ~90% U-235 [3]) with dU towards thermal fission fuel (~4% U-235 equivalent) is possible, this would consume only ~55 kt dU. The dU is therefore regarded as being a zero value asset [4] and may require long-term storage or disposal. In most nuclear states, some 80% of legacy dU is stored as uranium hexafluoride (UF_6) [1]; a hygroscopic crystalline solid that reacts violently with moisture to release highly chemo-toxic uranyl and hydrogen fluoride.

Currently, dU disposal is envisioned to be within deep cementitious geological disposal facilities (dGDF) [5]. The majority of dGDF post closure safety cases predict infiltration of groundwater, resulting in dissolution/re-precipitation of radionuclides present in the waste packages. This precludes direct dGDF disposal as a viable option for UF_6, instead deconversion to U_3O_8 may be achieved through steam quench-calcination processes [6].

The majority of ILW will be encapsulated in Portland grouts and contained in stainless steel drums. When a dGDF is re-saturated with groundwater, Na, K and Ca ions will be released into pore-water and near-field groundwater. Dissolution of K/Na hydroxide will initially alkalise groundwater towards pH 13.5, which is then buffered towards pH ~12.5 by Portlandite present in grouts. This hyperalkaline plume will be enriched with radionuclides such as Cs, Sr and more so uranium as the largest radionuclide faction by mass. Although U(VI) exhibits low solubility under these pH 12.5–13.5 conditions, its ubiquity in the dGDF will increase U(VI) concentrations. U(VI) is present in almost all aqueous solutions as the uranyl ion (UO_2^{2+}) which forms uranyl hydroxide clusters in the presence of hydroxyl ions [7–9]. Subsequent inorganic polymerisation will result in nucleation of uranyl hydroxide precipitates that crystallise with aging towards uranyl oxide hydrates (Schoepite, *meta*-Schoepite [10]:

* Corresponding author.
E-mail address: pmwd@leeds.ac.uk (W. Ding).

http://dx.doi.org/10.1016/j.jallcom.2016.07.140

$$U^{IV}O_{2(s)} \xrightarrow{Oxidation} U^{VI}O^{2+}_{2(s)} \xrightarrow{Dissolution} UO^{2+}_{2(aq)} \xrightarrow{Hydration/hydroxylation} Metal\ \ uranates \quad (1)$$

Incorporation of background cations will cause phase alteration [11,12] towards Ca/Sr-Becquerelite [13] or solubility-controlling uranates ($CaUO_4$, CaU_2O_7) [14,15]. These geologically persistent U(VI)-phases could further sequester key radionuclides (e.g. Cs, Sr, Np), affecting the long-term safety case of a dGDF [16–19].

Whilst crystalline metal uranates may become a suitable wasteform for permanent disposal or interim storage of uranic wastes, their synthesis pathways are often limited in the literature to ceramic methods involving direct calcination. Poor mixing between uranium and alkali metal salt particles will result in repeated grinding and prolonged calcination at high temperatures being required; reducing the overall process efficiency. Despite this, the ease of tuning Ca/U stoichiometry has resulted in the successful synthesis of Ca-uranates with Ca/U ratios of 0.25 [20], 0.5 [21], 0.337 [20], 1 [22], 2 [23], 3 [24]; in addition to other alkali uranates [25–27].

Sol-gel or co-precipitation chemistry is an attractive solution based route to synthetic metal oxides [28,29] that are low cost and typically require low temperatures, making processing convenient whilst also permitting control of particle morphology via frameworking agents [30]. Traditionally, metal alkoxides are used as solution phase precursors that readily undergo condensation [31] which may be expensive or complex to prepare as well as being heat, moisture and photo- sensitive. With the exception of titanium and zirconium alkoxides, most transition and actinide metal alkoxides are commercially unavailable.

Inorganic uranyl salts have been used during the synthesis of UO_2, U_3O_8 and UO_3 via direct [32] or indirect [33] alkalisation of uranyl nitrate solution. Precipitates are often amorphous, requiring calcination at 600 °C to crystallise the anhydrous uranium oxides [34,35].

Thus far, sol-gel syntheses have only been used to explore pure uranium oxides, whilst uranates have been formally explored only via the aforementioned anhydrous processes [36]. This study explores a simple and rapid aqueous based route towards calcium uranate particles, with potential for integration with current uranic waste stabilisation or dUF_6 deconversion processes [37]. It forms part of an effort to understand the underlying mechanisms leading to aqueous nucleation of hydrous metal uranates, whilst defining changes in their chemo-physical properties during anhydrous crystallisation.

2. Experimental

2.1. Materials and preparation

All reagents were of Analar grade and used as supplied without further purification.

Uranyl nitrate stock solution A 1.04 M uranyl nitrate solution was prepared by dissolving 1.51 g of uranyl nitrate hexahydrate ($UO_2(NO_3)_2 \cdot 6H_2O$, BDH Laboratory supplies) in 2.89 ml of deaerated deionised water (18 MΩ) to form a clear bright yellow solution.

Calcium nitrate stock solution: 0.28 g of calcium nitrate tetrahydrate ($Ca(NO_3)_2.4H_2O$, BDH Laboratory supplies) was added to 1.145 ml of deionised water to give a 1.04 M solution.

Calcium hydroxide stock solution: 0.7 g of calcium oxide (CaO, Sigma Aldrich) was added to 1 l of deaerated water (20 min N_2 sparged) in a stirred borosilicate Duran bottle. After solution becomes clear, a sealed cellulose semi-permeable tube containing 3 g/ml calcium hydroxide slurry was added to the solution and allowed to equilibrate to ~ pH 12.5 over 14 days at 20 °C.

Experimental procedure: In a typical synthesis, a 2.29 ml calcium enriched uranyl solution was prepared from mixing 1.145 ml of calcium and 1.145 ml of uranyl stock solutions to give 2.29 ml of preliminary reaction solution (pH 1.5) at 0.52 M: 0.52 M U(VI):Ca(II) concentrations respectively. To this initial solution, saturated calcium hydroxide solution was added slowly dropwise under vigorous stirring until pH 12 was reached. The reaction mixture was centrifuged at 14400 *g* for 3 min to collect and pelletize the bright orange precipitate. The remaining colourless clear supernatant was removed with pipette. The precipitated particles were rinsed with DI water and pelletised. The rinsed solids were re-suspended in 40 ml of propan-2-ol and centrifuged to prevent further ripening/hydrolysis reactions via displacement of surface water with alcohol groups. This was repeated twice and the solids were concentrated into 5 ml of propan-2-ol for storage, allowing rapid drying prior to analysis using the methods described below.

2.2. Sample analyses

Quartz crystal microbalance (QCM) A chrome-gold quartz crystal (d = 25.4 mm) (Stanford Research Systems, Sunnyvale, California) was rinsed using Millipore water followed by isopropanol then air dried. The crystal was mounted onto a 5 MHz Stanford Research Systems QCM200 probe and the sensor was left to reach a stable frequency and resistance reading in air, then repeated upon submersion in the stirring reaction solution. A shift of at least 0.75 Hz h^{-1} and 0.34 Ohm hr^{-1} in air and 3 Hz h^{-1} and 1.65 Ohm hr^{-1} in solution was considered stable. Calcium hydroxide solution was added to the reaction solution until pH 12 and the frequency and resistance data was recorded throughout the process.

Zeta potential measurements Precipitates were disaggregated using pestle and mortar then suspended in deionised water (18 MΩ). Remaining aggregates were allowed to settle and aliquots of the suspended fraction were added to prepared pH solutions buffered using 0.1 M HNO_3 and $(CH_3)_4NOH$ solutions to a final concentration of ~1000 ppm immediately prior to measurement. Triplicate samples were loaded into folded capillary zeta cells then analysed using a Malvern Instruments Zetasizer Nano. The refractive index was taken to be 1.63 (see Dynamic light scattering measurements below).

UV–Vis analyses Aliquots of reaction solution were removed at selected solution pH values followed by centrifugation to pelletize solids. The supernatant was removed and their single wavelength optical absorbance measured using a Jenway 6715 spectrophotometer to follow changing solution absorption throughout the reaction. 414 nm was found to be the maximum absorbance peak (A414) in a UV–Vis spectrum of stock uranyl nitrate solution at ~ pH 2.

The raw total spectrophotometric absorbance at 414 nm (A414) of the pelletised reaction aliquots was treated by subtracting the A414 of $UO_2(NO_3)_2$ solution of equivalent dilution to isolate ΔA414 due to variation of U(VI) speciation. This treated data was then fitted using a Gaussian function to guide the eye (Fig. 4a black square, Gaussian fit in dashed black). Fresh solutions were prepared

at 0.01 M initial U(VI) concentration to pH 2–5 and their UV–Vis spectra collected between wavelength range of 350–500 nm (Fig. 4b).

Dynamic light scattering (DLS) Ex-situ DLS measurements were made using a 532 nm Nd:YAG laser and a Brookhaven digital correlator (BI-9000AT) controlled using the 9KDLSW data recording and analysis software package. The precursor Ca/U solution was filtered using a 0.22 μm syringe filter and the reaction vessel covered to reduce dust contamination. As the reaction proceeded, aliquots of reaction solution were extracted at 0.5 pH intervals from pH 2 until pH 5.5. A refractive index of R = 1.63 was derived for the particles via the Gladstone-Dale [38] relationship [39,40] (see Supplementary materials). Refractive energies used for the constituents UO_3, CaO and H_2O were included from literature [40] and the particle density was assumed the same as the closely related $CaU_2O_7.1.7H_2O$ (4.9 g cm^{-3}) [41].

Thermal analyses: Thermogravimetric and Differential Scanning Calorimetry analysis (TGA-DSC) was performed using a Mettler-Toledo TGA-DSC1 instrument on the solids to observe mass loss during calcination under a flow of N_2 gas at 50 cm^3 min^{-1}. In total, ten samples were analysed at different temperatures ranging between 50 °C and a maximum temperature, T_{max}, with T_{max} increasing in 100 °C increments between 100 and 1000 °C. These samples were placed in a 70 μl alumina crucible. The heating rate of the analyses was at 10 °C min^{-1} and the samples were held in isothermal plateau at the T_{max} for 300 min. All TGA-DSC data were blank subtracted and then derived with respect time to over a region of 20 data points to give the corresponding DTG trace (Fig. 7).

X-Ray Diffraction (XRD) analyses Calcined samples were pulverised and analysed on a Bruker D8 Diffractometer equipped with Cu Kα x-ray source and lynx eye detector. A hydrous sample (Fig. 8a, 25 °C) was dried after 7 days of storage under IPA, then pulverised and analysed in the same manner as for the calcined samples. XRD patterns were compared to International Centre for Diffraction Data (ICDD) powder diffraction file database (PDF+4). The 25–600 °C XRD patterns were treated using a quadratic polynomial Savitzky-Golay filter [42] (10 point window) to improve data clarity in poorly crystalline samples that required no further analysis. Quantitative phase compositions were determined using the Rietveld method [43,44] via the X'Pert Highscore Plus software using available crystal structural data for $CaUO_4$ and UO_2.

SEM analyses Solid samples were carbon coated and imaged using a FEI Quanta FEG 650 Environmental Scanning Electron Microscope (ESEM) equipped with an electron microprobe. EDS spectra were collected from a minimum of 3 regions per sample. The AZTEC software package was used during standardless quantification of Ca and U elemental concentrations.

TEM analyses Particle suspensions were dried onto amorphous carbon support copper grids prior to imaging using a FEI Tecnai TF20 FEGTEM. ImageJ [45] was used to measure particle size and lattice fringe spacing via Fast Fourier Transform patterns (FFT).

ICP-OES analyses 0.5 ml aliquots were removed from the reaction vessel and immediately passed through a 0.22 μm pore size filter and then centrifuged at 14400 *g* for 5 min. The supernatant was acidified overnight using Aristar HNO_3, diluted to 1 wt% acid concentration (~50 ppm U) and used for uranium ICP-OES analysis on a Thermo iCAP 7400 instrument. The solids from the TGA analyses were digested using a 100 μL aliquot of 70% nitric acid, then diluted as for the solution samples. All samples were calibrated against calcium-uranium standards containing Yttrium as an internal standard.

3. Results

3.1. Thermodynamic modelling

The distribution of U(VI) species in aqueous solution was calculated using the software package PHREEQC [46,47] loaded with the ANDRA ThermoChimie database [48] and updated thermodynamic data for uranium [49,50]. Additional K_{sp} data was inserted into the working database to include an amorphous Schoepite phase [51]. Specific ion-interaction theory (SIT) was used for ionic strength corrections. Percentage speciation for Ca and U(VI) and relevant crystalline phase saturation indices (SI) are presented (Fig. 1). The latter being a logarithmic relationship between ion activity product (IAP) of dissolved species and solid phase solubility product (K_{sp}) to give phase saturation index (SI), where phase SI > 0 represents supersaturation; SI < 0 represents undersaturation and SI = 0 represents phase equilibrium between dissolution and precipitation.

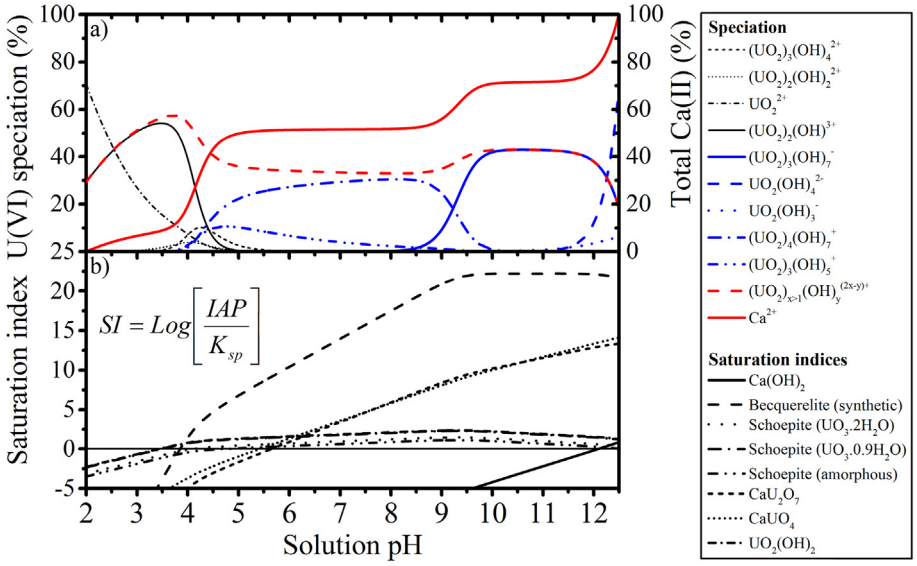

Fig. 1. PHREEQC reaction model of a) major total U(VI) (left axis) and Ca(II) (right axis) speciation by percentage at 20 °C. b) Relevant saturation indices of solid phases (left axis) and total dissolved U(VI) content (right axis).

Accordingly, the calculations show that the precursor solution is dominated by uncomplexed UO_2^{2+} and binuclear $(UO_2)_2OH^{3+}$. UO_2^{2+} is consumed with increasing solution pH towards 2.5 and less rapidly from pH > 3 until complete consumption by pH 5. Between pH 2–5, concentration maxima in U(VI) hydroxides occur at solution pH values of 3.5 $[(UO_2)_2OH^{3+}]$, 4.1 $[(UO_2)_2(OH)_2^{2+}]$, 4.3 $[(UO_2)_3(OH)_4^{2+}]$ and 4.8 $[(UO_2)_3(OH)_5^{+}]$ respectively and is reflected in a pH 3.75 maxima in total polymeric U(VI) hydroxides. There is also a rapid incremental increase in expected Ca concentration between pH 3.5 (0.42 mol l^{-1}) and pH 5 (0.74 mol l^{-1}). Whereby the solution becomes supersaturated with respect to crystalline uranyl oxide hydrates (pH 3.5: $[UO_3(0.9–2)H_2O]$; pH 3.9: [Becquerelite]; pH 4.1: $[UO_2(OH)_2]$). The continued increase in Ca and OH^- concentration results in solution supersaturation in $CaUO_4$ and CaU_2O_7 whilst the $[(UO_2)_4(OH)_7^+]$ dominated region (pH 4.5–9) is rapidly exchanged for anionic $[(UO_2)_3(OH)_7^-]$ at pH 9.2. Excess OH^- in solution leads to depolymerisation of $[(UO_2)_3(OH)_7^-]$ to form monomeric hydroxides $[UO_2(OH)_3^-]$ and $[UO_2(OH)_4^{2-}]$.

3.2. QCM measurements

During alkalisation of the initially bright yellow transparent precursor solution (Fig. 2 circlet 1) by addition of clear transparent $Ca(OH)_2$ solution, a diminished change occurs in the frequency (ΔF) and resistance (ΔR) shifts up to pH 4.8. The almost linear decrease in ΔF is reflected by an opposing increase in ΔR in this region and a progressive yellowing of the transparent solution. This 40 Hz (9%) reduction in ΔF (Fig. 2 solid line) corresponds to a comparatively minor +0.56 Ω (1.6%) increase in ΔR (proportional to vibrational dissipation [52]) and allows use of the Sauerbrey relationship [53,54] to approximate an average mass of a rigidly adsorbed and evenly spread thin-film on the QCM crystal surface to ~3.5 μg. Using database values for the densities of Schoepite (ICSD 82477, ρ = 4818.64 kg m^{-3} and Metaschoepite (ICSD 23647, ρ = 8017.66 kg m^{-3}), an average film thickness of an adsorbed layer would range between 0.87 and 1.45 nm. A sharp increases in ΔF and ΔR gradients (dΔF, dΔR) coincide with the solution becoming visibly opaque (Fig. 2* circlet 2) at pH 4.8. Subsequent reductions in dΔF/dΔR occur at pH 5.8 and pH 6.8 respectively to reach a plateau between pH 6.8 and pH 7.5, whilst the suspension darkens in colour. A final progressive increase in dΔF and dΔR up to pH 12 occurs with the formation of a clear colourless supernatant layer above the agitated particle bed.

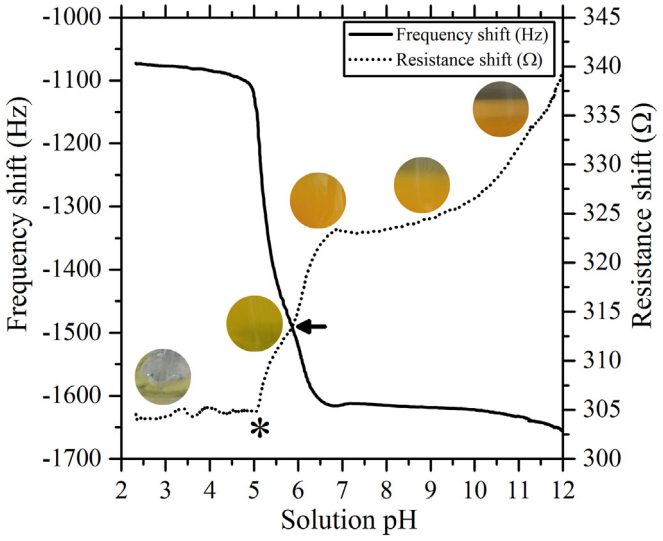

Fig. 2. QCM frequency and resistance shift as a function of solution pH; with asterix (*) representing the visible solution cloud point. Image circlets are ordered from left-right as 1–5; and show (1) initial uranyl nitrate solution followed by addition of calcium hydroxide titrant until (2) solution clouding point, (3) gelation, (4)–(5) collapse and settling.

3.3. Zeta potential (ZP) measurements

A point of zero charge (PZC) (Fig. 3) was found for the precipitated particles at pH 4.1 regardless of electrolyte concentration in the aqueous matrix. However relative differences become immediately apparent in their rates of change by pH 4.8 (−16.2 and −8.0 mV respectively), resulting in a more negative pH 12 ZP for the pure water suspension (−35.7 mV) compared to the 0.01 M NaCl suspension (−22.0 mV). ZP trends for both suspensions coincide with similar hydrous divalent (Mg, Mn, Ni) uranium oxides.

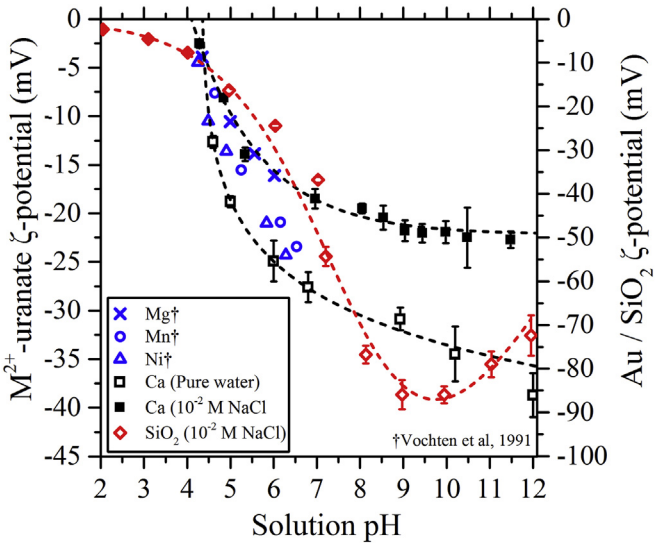

Fig. 3. Particle zeta potential of hydrous Ca–U(VI) oxide as a function of solution pH in DI water and 0.01 M NaCl; other divalent metal U(VI) oxides from Vochten et al. (blue) [55] and SiO_2 particles 0.01 M NaCl solution respectively are included for reference. (For interpretation of the references to colour in this figure legend, the reader is referred to the web version of this article.)

3.4. UV–vis absorbance

Solution aliquots develop in total absorbance between pH 3–5.7 before increasing rapidly at pH 5.7 towards a final plateau between pH 6–12. The centrifuged reaction aliquots (Fig. 4a, black squares) exhibit a Gaussian shaped absorbance peak centred at pH 4.5 with a peak width of 3 pH values, no further changes in absorbance is apparent after pH6. The absorbance spectra of samples before the cloud point (pH 5.5) between pH 2–3.5 (Fig. 4b) shows that A_{max} remains constant up to pH 3 (Fig. 4b). They are characterised by three major A_{max} at (i) 403, (ii) 413.8, (iii) 426 nm with shoulders at 392 nm and 438 nm is consistent with previous spectroscopic data for the UO_2^{2+} ion [56]. The pH 3.5 spectrum is characterised by broadened peaks, though maintains the three A_{max} observed at lower pH values. Higher pH spectra (Fig. 4b, pH 4–5) show consistently broadened characteristics whilst completely shifting the A_{max} peaks to 421.8 nm and 429 nm. U(VI) speciation data (Fig. 1a, black lines) reveals a solution dominated by $[UO_2^{2+}]$ ions up to pH 3, followed by formation of $(UO_2)_2(OH)_2^{2+}$ up to its maximum

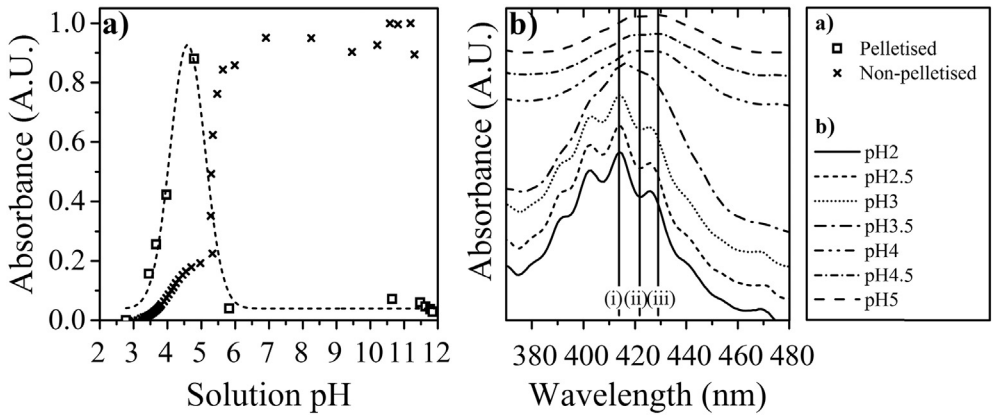

Fig. 4. (a) Spectrophotometric absorbance at 414 nm of pelletised (black square) and non-pelletised (black cross). (b) Stacked ex-situ UV–Vis spectra of reaction aliquots with vertical solid lines showing the wavelengths of absorbance maxima for the U(VI) species (i) UO_2^{2+}, (ii) $(UO_2)_2(OH)_2^{2+}$ and (iii) $(UO_2)_3(OH)_5^{+}$.

at pH 4 and subsequently by the higher uranyl hydroxylation products [$(UO_2)_3(OH)^{5+}$] and [$(UO_2)_4(OH)^{7+}$] up to pH 5.

3.5. ICP-OES analyses

Approximately 10% of initial U and Ca is removed simultaneously from solution up to pH 5 whilst the [Ca/U] ratio of filtered solids reach unity. Between pH 5–7, almost complete removal of uranium is occurs whilst an additional ~48% Ca is gradually removed up to pH 12 to yield a final expected [Ca/U] ratio of ~0.6. The average calcium to uranium molar ratios of precipitates calcined between 25 and 1000 °C (25 °C sample represents the untreated precipitate) were also analysed after dissolution in 1% HNO_3 acid to give Ca/U = 0.68 ± 0.043 (Ca:U ~ 0.25:0.38) or a calculated stoichiometric formula of $Ca_2U_{2.92}O_{10.77}$.

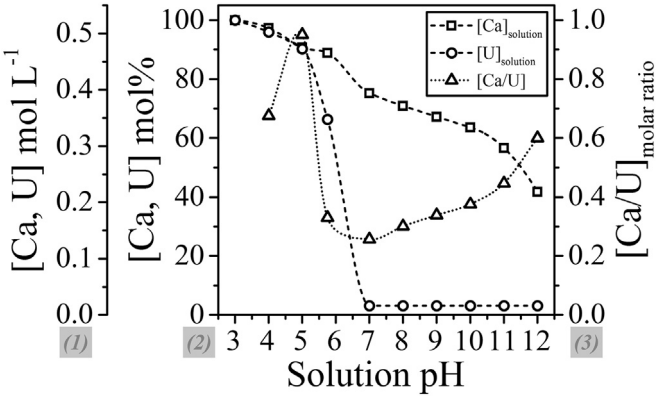

Fig. 5. Change in concentration of U and Ca remaining in solution as *(1)* mol l^{-1}; *(2)* mol%, and *(3)* molar [Ca/U] ratio of removed solids (triangles) with respect to solution pH.

3.6. Dynamic light scattering

Dynamic light scattering performed on a range of 0.066 M/0.01 M Ca/U(VI) nitrate solutions buffered between pH 2–5.5 using HNO_3 and $(CH_3)_3NOH$, though only the pH 5–5.5 sample yielded scattered light count rates above background. Fig. 6 shows that non-regularised (NNLS) and regularised (CONTIN) least squares fitting yielded a pH 5.5 particle size distribution (PSD) that is characterised by three major particle size populations that

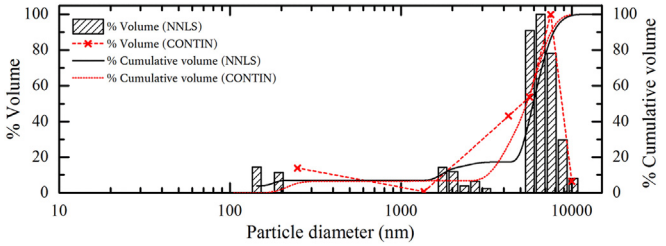

Fig. 6. Distribution of hydrodynamic particle diameters in pH 5.5 solution as a function of %volume received from NNLS (shaded black bars) and CONTIN (red crosses) fitting methods. (For interpretation of the references to colour in this figure legend, the reader is referred to the web version of this article.)

approximately corroborate between the two data fitting methods; [NNLs, CONTIN] hydrodynamic diameter = [144–193, 248 nm], [1750–3160, 1370 nm] and [5680–10240, 4260–10000 nm]. These correspond to d50s by volume as d_V50_{NNLS} = 5550 nm, d_V50_{CONTIN} = 5150 nm respectively.

3.7. Thermogravimetric analysis

Fig. 7 shows ~10% weight loss occurs when samples were heated from 50 °C to 1000 °C and the samples appeared to follow a 5 - region weight loss profile outlined below:

Region 1 – an initial steep ~5.80% (6.63 mg) weight loss region between 50 and 175 °C with mild endothermic heat flux, which is reflected as a double minima in the DTG trace as two changes in weight loss regime within this region. Isothermal weight loss is highest in this range (Fig. 7, insert).

Region 2 – a lesser ~3.94% weight loss region between 175 and 700 °C which appears as a broad depression in the DTG trace, whilst isothermal weight loss stabilises. Particles deepen in colour to ochre from light orange.

Region 3 – samples became progressively darker in orange with increasing temperature until an ochre colouration is reached between 700 and 800 °C; where the ochre colouration is intermixed with dark green specks. Dynamic weight loss over this range is diminished, whilst isothermal weight loss begins to rise.

Region 4 – a ~1.55% weight loss region between 800 and 950 °C this facile weight loss is reflected in a sharp depression in the DTG trace over the same temperature range and is accompanied by a change in colouration towards a green tinged black;

Region 5 – a secondary weight loss plateau beyond 950 °C accompanied by darkening of colour until a lustrous black solid of a

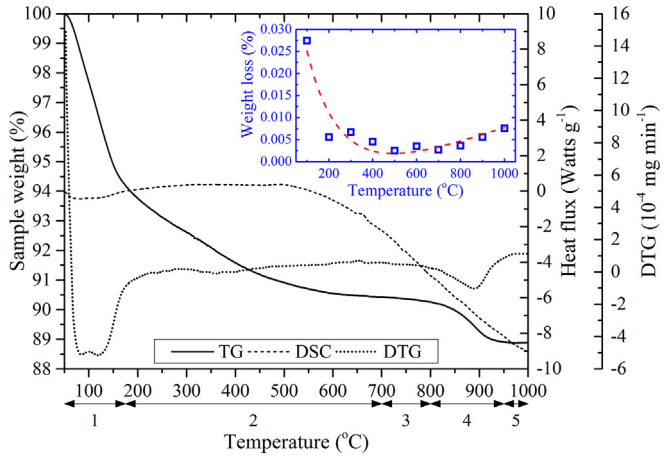

Fig. 7. Dynamic heat treatment profile of samples in the temperature range 50–1000 °C, showing normalised thermogravimetric (TG), derivative TG (DTG) and differential scanning calorimetry (DSC) traces; with mass loss regions 1–5 labelled accordingly. The insert (blue) shows total isothermal weight loss over 300min with a fitted Log normal curve for guidance (red dashed). (For interpretation of the references to colour in this figure legend, the reader is referred to the web version of this article.)

3.8. XRD analysis

Sample pXRD patterns (Fig. 8a, 25 °C) below 700 °C show poor peak definition with broad intensity maxima resembling those of $Ca_{1.5}U_6(OH)7O_{16}.7H_2O$ [57]. Calcination of samples in a N_2 atmosphere up to 700 °C results in gradual increase in peak definition towards a $Ca_2U_3O_{11}$ phase. The samples calcined to 1000 °C match database peak maxima for $CaUO_4$ and UO_2.

Phase quantification for the 900 °C sample was attempted using the Rietveld method [43,44] with known structural data for UO_2 (PDF: 04-008-7779) and $CaUO_4$ (PDF: 04-007-9392). This yielded weight percentages for UO_2 and $CaUO_4$ of 34.4 wt% and 65.6 wt% respectively and a calculated bulk [Ca/U] stoichiometry of 0.601 ($Ca_2U_{2.3}O_{12}$). Parameters refined were specimen displacement, background, scale factor, unit cell parameters, peak shapes, W and U profile parameters. Goodness of Fit (GOF, χ^2) and R weighted profile (R_{wp}) values were monitored to improve the refinement. R and refined unit cell parameters are summarised in (Fig. 8). As structural data is unavailable for $Ca_2U_3O_{11}$, structural refinement was not attempted on the 700 °C XRD pattern.

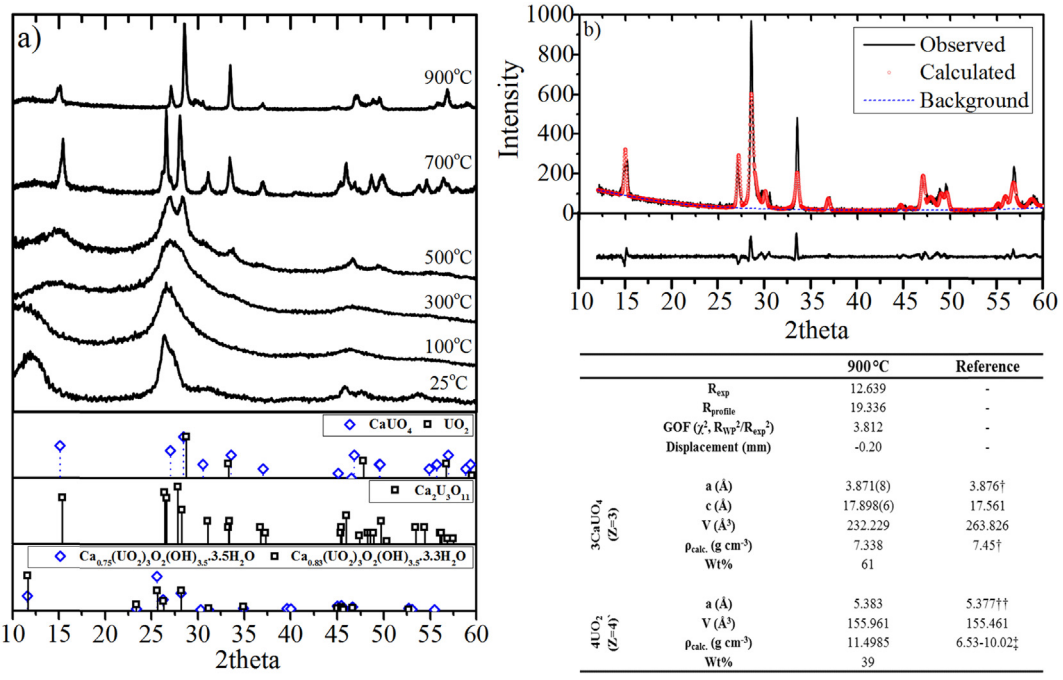

		900 °C	Reference
	R_{exp}	12.639	-
	$R_{profile}$	19.336	-
	GOF (χ^2, R_{WP}^2/R_{esp}^2)	3.812	-
	Displacement (mm)	-0.20	-
3CaUO$_4$ (Z=3)	a (Å)	3.871(8)	3.876†
	c (Å)	17.898(6)	17.561
	V (Å^3)	232.229	263.826
	$\rho_{calc.}$ (g cm^{-3})	7.338	7.45†
	Wt%	61	
4UO$_2$ (Z=4)	a (Å)	5.383	5.377††
	V (Å^3)	155.961	155.461
	$\rho_{calc.}$ (g cm^{-3})	11.4985	6.53-10.02‡
	Wt%	39	

Fig. 8. (a) Selected powder XRD patterns of particles heat treated between 25 °C (precipitate) and 900 °C; and PDF-4+ database reference patterns for $Ca_{0.75}(UO_2)_3O_2(OH)_{3.5}.3.5H_2O$ [PDF 00-047-0496], $Ca_{0.83}(UO_2)_3O_2(OH)_{3.5}.3.3H_2O$ [PDF 00-050-0039]; $Ca_2U_3O_{11}$ [PDF 00-045-0008]; $CaUO_4$ [PDF 04-007-5327] and UO_2 [PDF 04-017-6940]; (b) Calculated (red), observed (black), background (blue) and residual plots for 900 °C Rietveld XRD data with refinement R factors and unit-cell parameters for 900 °C and corresponding reference values for †$CaUO_4$ (PDF: 04-007-9392) [22] and ††, ‡UO_2 (PDF: 04-017-6940) [58,59]. (For interpretation of the references to colour in this figure legend, the reader is referred to the web version of this article.)

brittle nature remained. A broad endotherm begins at 600 °C (*Regions 3*) until *Region 5* does not coincide with specific weight losses. Isothermal stability decreases linearly from the Region 2 minima up to region 5.

As carbon dioxide was excluded from precursor solutions and the reaction vessel, the gaseous decomposition product was assumed to be water. Mass loss was therefore used to calculate molar water loss and incorporated into the stoichiometric formulae as H_2O and OH groups for clarity (see Equations (2)–(5)).

3.9. SEM and TEM imaging

TEM micrographs are presented in Fig. 9 of the solids extracted from the reaction solution at three pH values after initial onset of precipitation. The solids appear to be composed of a network of randomly distributed nanoparticle aggregates that warped during imaging for the pH 5.5 and to a lesser degree for the pH 8.5–11 aggregates. Size measurement of particles with coherent lattice fringes (Fig. 9 circlets) revealed their diameters to be 14.06 ± 2.25 nm, 12.06 ± 2.14 nm and 9.17 ± 1.49 nm for pH 5.5, 8.5

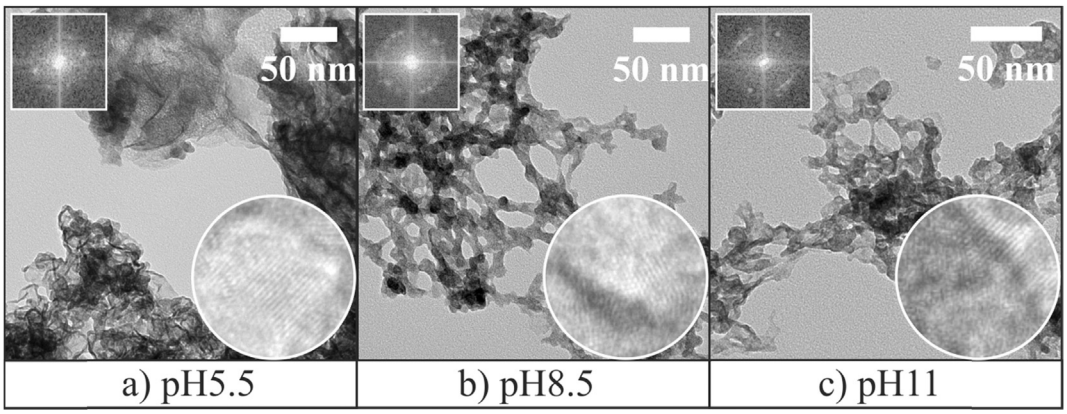

Fig. 9. TEM micrographs of dried calcium uranate aggregates extracted from three pH solutions to show nanoscale particle morphology. Circlets are magnified single particle images (d = 10 nm) and square insets are Fast Fourier Transform (FFT) patterns of respective circlets.

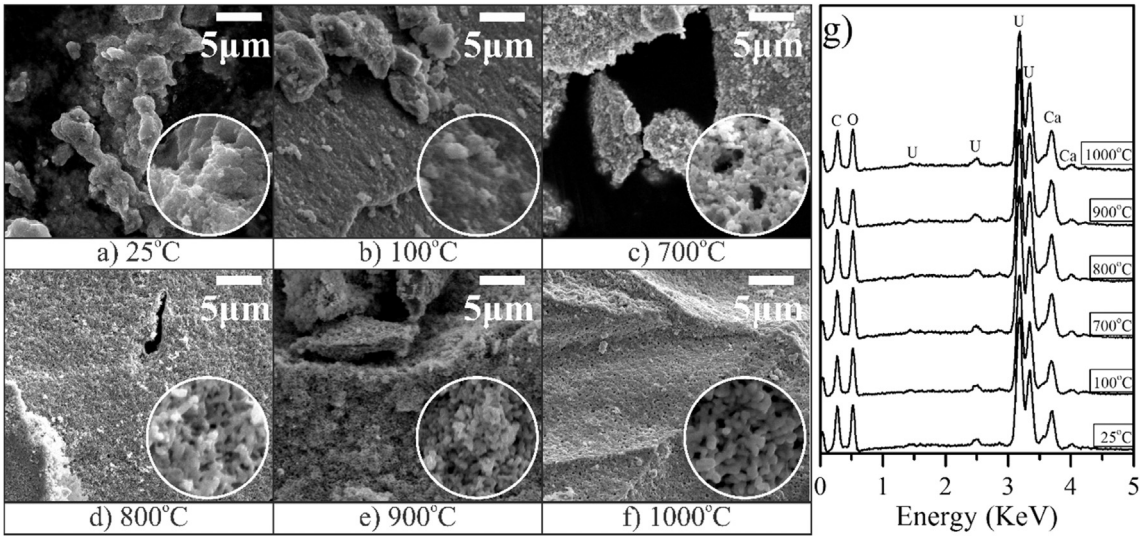

Fig. 10. SEM micrographs of selected samples heat treated at temperatures between 25 °C and 1000 °C to show meso-scale particle surface morphology. Circlets highlight micro-scale morphology and are 2 μm diameter. a) Poorly-ordered Ca-uranate; b) dehydrated precipitate at 100 °C; c) Ca-uranate $Ca_2U_3O_{11}$; d) - f) Ca-monouranate and U(IV)-oxide particles $CaUO_4$, UO_2; g) Corresponding EDS spectra of samples a) – f).

and 11 samples respectively. The rectangular crystallites had average geometric anisotropy ratios (length/width) of 1.9 ± 0.2, 2.0 ± 0.4 and 2.1 ± 0.3 respectively. Inspection of the FFT interference patterns (Fig. 9 square inserts) derived from particle lattice fringes reveal spacings in order of decreasing intensity 3.1–3.3 Å, 2.6–2.7 Å and in the pH5.5 solids, also at 1.8–1.9 Å; corresponding approximately with the d - spacings for the (−111), (111) and (−311) diffraction peaks of crystalline $Ca_2U_3O_{11}$.

SEM photomicrographs of the 25 °C and 100 °C (Fig. 10a, b) samples show irregular shaped and sized aggregates with average cluster diameters of ~146 nm and ~151 nm respectively. Between 700 and 900 °C, particle diameters decrease in 100 °C increments to ~140, ~124 and ~113 nm accompanied by an observable alteration from smooth spheroids at 700 °C towards spherical particle aggregates by 900 °C interspersed by an increasingly regular pore size distribution. By 1000 °C (Fig. 10f), particle surfaces become smoother and consist of fused spherical particles of ~118 nm interspersed with larger pores. Standardless quantification from EDS data (Fig. 10g) across all samples revealed calcium, uranium and oxygen atom percentages of 11.4 ± 1.2, 18.2 ± 1.9 and 70.3 ± 3.2 respectively and a Ca/U stoichiometry of 0.63 ± 0.02 ($Ca_{1.9}U_{3.01}O_{10.95}$).

4. Discussion

4.1. Hydrous calcium uranate condenses from clusters of U(VI) hydroxide oligomers

The initial reaction solution is predicted to contain monomeric and partially hydrolysed U(VI) species as UO_2^{2+} or $(UO_2)_2OH^{3+}$ and dissociated calcium as Ca^{2+}. The former is responsible for the low initial pH of the precursor solution (~pH 2) as described by a proton release equilibria (Equation (2)) occurring during hydrolysis [60–62].

$$xUO_2^{2+} + yH_2O \Leftrightarrow (UO_2)_x(OH)_y^{(2x-y)+} + \left(yH^+\right) \quad (2)$$

A progressive increase in hydroxide in solution during $Ca(OH)_{2aq}$ addition consumes protons to drive kinetic olation between uranyl ions towards oligomeric U(VI) species ($(UO_2)_2(OH)_2^{2+} \rightarrow (UO_2)_3(OH)_4^{2+} \rightarrow (UO_2)_3(OH)_5^{+}$). This is supported by a shift in the observed UV–Vis spectra (Fig. 4b) from a uranyl towards a U(VI)

hydroxide (UOH) dominated system above pH 3 (Fig. 4b). Due to the 10 and 49 fold greater molar absorptivity of the polymeric uranyl hydroxides $(UO_2)_2(OH)_2^{2+}$ (101 ± 2 mol^{-1} cm^{-1}) and $(UO_2)_3(OH)_5^+$ (474 ± 7 mol^{-1} cm^{-1}) compared to UO_2^{2+} (9.7 ± 0.2 mol^{-1} cm^{-1}) [56], the progressive increase in UOH concentration may be followed via spectrophotometric absorbance measurements (Fig. 4 black).

The variation between the $A414_{pelletised}$ and $A414_{non\text{-}pelletised}$ samples indicate some removal of U(VI) solids from solution above pH 4.8 (Gaussian fit maxima) and almost complete removal by pH 5.5. However the approximate minimum particle size that may be centrifugally removed from solution is ~44–62 nm (see Supplementary materials) whilst primary crystallites are ~14.06 nm (Fig. 9a). Therefore the increase in overall $A414_{pelletised}$ between pH 2–4.8 may be due to both non-aggregated nanoparticles and U(VI) hydroxides (Fig. 4b).

The 0.87–1.45 nm film deposited onto the QCM crystal surface below the cloud point (Fig. 2, pH 5) contains both U and Ca according to ICP-OES (Fig. 5); and could in part, be due to the $SiO_{2(s)}$-$UO_2^{2+}{}_{(aq)}$ inner – sphere complexation observed in aqueous U(VI)-silicate systems [63,64] that appears unaffected by $[Ca^{2+}]$. Continuing pH elevation functionalises the deposited $SiO_{2(s)}$-$UO_2^{2+}{}_{(aq)}$ layer with higher [63] oligomeric U(VI) hydroxide clusters, trapping Ca^{2+} ions in a similar manner to the dynamically ordered liquid-like oxyanion polymers that form prior to calcium carbonate nucleation [65].

Both deposited and solution phase Ca–U(VI) clusters subsequently undergo rapid crystallisation to primary crystals (Fig. 9a) towards pH 5 driven by increasing supersaturation in oligomeric U(VI) hydroxides. Rapid isotropic aggregation [66] occurs simultaneously with nucleation due to the PZC lying at ~ pH 4.3 (Fig. 3 black squares) resulting in the apparent large discrete aggregates (d_V50 = 5.15–5.55 μm) detected at pH 5.5 (Fig. 6). In accordance with the Ostwald step rule [67], a reduction in system Gibbs energy via the shortest reaction pathway favours the formation of less stable and poorly crystalline phases [68,69]. The ICP-OES data (Fig. 5) shows a Ca/U stoichiometry of ~1, implying that $CaUO_4$ crystallises (~pH 5) rather than the expected Becquerelite (Fig. 1b).

The system transitions at pH 6 (Fig. 2 arrow) from a suspension of discrete aggregates (Fig. 6) to a Ca-deficient ([Ca/U] ~ 0.26) gel at pH 6 via removal of 87 mol% solution U(VI) (Fig. 5, black circle). This gel continues to uptake Ca from solution as a function of pH (Fig. 5) and Ca solubility (Fig. 1, SI: $Ca(OH)_2$) towards poorly-crystalline (Fig. 8a, 25 °C) particles (d ~ 9 nm) with a final Ca/U ratio of ~0.67 (Fig. 5, pH 12). This phenomena, common to hydrous U(VI) phases [69–71], is facilitated by a labile 1:2 $[Ca^{2+}]$: $[H_3O^+{}_{lattice}]$ ion-exchange mechanism [55] and may be accommodated by minor crystallite lattice distortions (Fig. 9).

4.2. Calcium uranate crystallises via concerted dehydroxylation-olation

The thermal decomposition resulting in particle mass losses (TG) up to 700 °C are due to dehydration processes [72,73] (see supplementary materials, Fig. 2). In TG region 1 (Fig. 7 50–175 °C), ~3.5 mol of H_2O are volatilised per mole $Ca_2U_3O_{11}$ (Equation (3)). The relatively low temperatures imply the presence of outer sphere complexation between molecular water and surface U(VI)-hydroxyl moieties. If hydrated uranates are intermediates between solvated U(VI) hydroxide clusters and crystalline U(VI) oxides [74], then this hydrogen-bound water is highly labile [75] and would require little structural or crystalline (Fig. 8a 25–200 °C) rearrangement to accommodate the change. Indeed there was little observed mesoscopic changes occurring in the particle morphology (Fig. 10a, b).

$$Ca_2(UO_2)_3O_{3.75}(OH)_{2.5}.3.5H_2O \xrightarrow{\Delta(25-200\,^\circ C)} Ca_2(UO_2)_3O_{3.75}(OH)_{2.5} + 3.5H_2O \quad (3)$$

Conversely, dissociative water sorption occurs via inner sphere complexation to uranyl centres along the equatorial plane, requiring more energy to achieve the observed 1.25 mol dehydroxylation between 200 and 700 °C (Equation (4)) during TG analysis (Fig. 7).

$$Ca_2(UO_2)_3O_{3.75}(OH)_{2.5} \xrightarrow{\Delta(200-700\,^\circ C)} Ca_2(UO_2)_3O_5 + 1.25H_2O \quad (4)$$

This conversion increases sample crystallinity (Fig. 8a, 700 °C) and therefore long-range structural order considerably, implying a concerted dehydroxylation – olation reaction between adjacent (UO_2)–OH groups. This phase development is accompanied by extensive particle shrinkage and solid state ripening processes to form the spherical particles and apparent porosity observed at 700 °C (Fig. 10d). Despite the hydrous Ca-uranate particles (Fig. 9c) being most consistent with the formula $Ca_{0.75\text{-}0.83}(UO_2)_3O_2(OH)_{3.5}.(3.3–3.5)H_2O$ (Fig. 8a), stoichiometric analysis ([Ca/U] ~ 0.64), FTIR analysis (supplementary materials, Fig. 2) and the early weight loss measurements (Fig. 7) discussed above indicate a structure with a lower overall water content and therefore a composition closer to $Ca_2(UO_2)_3O_{3.75}(OH)_{2.5}.3.5H_2O$.

The colour change to black in TG region 4 suggests a U(VI)→U(IV) reduction accompanied by microscale structural changes (Fig. 10d–f). This transition may be accommodated by conversion of $Ca_2U_3O_{11}$ to biphasic $CaUO_4$ and UO_2 particles (Fig. 8a, 900 °C) via dissociation of 0.5 mol oxygen (Equation (5)) implying that a higher Ca-loading towards [Ca/U] = 1 would increase thermal stability.

$$Ca_2(UO_2)_3O_5 \xrightarrow{\Delta(700-1000\,^\circ C)} 2Ca\left(U^{VI}O_2\right)O_2 + U^{IV}O_2 + \frac{1}{2}O_2 \quad (5)$$

Whilst the presence of green specks at 800 °C could indicate partial reduction to $Ca_2U_3O_{10}$ [76], the relative thermal stability of $Ca_2U_3O_{11}$ (Fig. 7, insert) in addition to requiring a reductive atmosphere precludes this pathway from being likely.

5. Conclusions and implications

The alkalisation of aqueous U(VI) – Ca(II) solutions results in hydroxylation of uranyl species towards oligomeric U(VI) clusters. The majority of U(VI) (~87 mol%) was removed from solution between pH 5–7 via nucleation into poorly-ordered nanoparticles of 14 nm. These Ca-deficient aggregates continued to uptake Ca until a final Ca/U ratio of 0.67 was reached. This hydrous calcium uranate ($Ca_2(UO_2)_3O_{3.75}(OH)_{2.5}.3.5H_2O$) underwent a two-stage dehydration-dehydroxylation between 100 and 700 °C under a redox-neutral atmosphere to form crystalline $Ca_2U_3O_{11}$; which subsequently decomposed into a biphasic $CaUO_4/UO_2$ mixture at 800 °C. The simple and rapid process studied here may be integrated with existing processes [37] to remove U(VI) from aqueous waste streams, whilst creating a crystalline low solubility uranate phase that may be used for long-term storage or permanent disposal of waste uranium.

Acknowledgements

The authors are grateful to the financial support from the EPSRC,

Nuclear Decommissioning Authority (NDA) and Sellafield Ltd for this work. Thanks are due to Yulong Ding of the University of Birmingham for numerous helpful comments and academic discussions throughout; Stephen Reid, Richard Walshaw and Michael Ward from the University of Leeds for their assistance with ICP-OES, SEM and TEM techniques respectively.

Appendix A. Supplementary data

Supplementary data related to this article can be found at http://dx.doi.org/10.1016/j.jallcom.2016.07.140.

References

[1] OECD, Management of Depleted Uranium: a Joint Report by the OECD Nuclear Energy Agency and the International Atomic Energy Agency, Organisation for Economic Co-operation and Development, France, 2001.
[2] OECD, Technology Roadmap Update for Generation IV Nuclear Energy Systems, OECD, 2014.
[3] IPFM, Global Fissile Material Report 2011: Nuclear Weapon and Fissile Material Stockpiles and Production, International Panel on Fissile Materials, 2011.
[4] NDA, Strategy: Effective from April 2011, UK, 2011.
[5] G.B.D.f. Environment, et al., Managing Radioactive Waste Safely: a Framework for Implementing Geological Disposal, Vol. 7386, The Stationery Office, 2008.
[6] A.M. Roach, Consideration of Safeguards Requirements during the Design of the URENCO Tails Management Facility, International Atomic Energy Agency, 2010.
[7] M.A. Denecke, Actinide speciation using X-ray absorption fine structure spectroscopy, Coord. Chem. Rev. 250 (7–8) (2006) 730–754.
[8] N. Mace, et al., EXAFS investigation on U(VI) immobilization in hardened cement paste: influence of experimental conditions on speciation, Radiochim. Acta 101 (6) (2013) 379–389.
[9] D.L. Clark, et al., Chemical speciation of the uranyl ion under highly alkaline conditions. Synthesis, structures, and oxo ligand exchange dynamics, Inorg. Chem. 38 (7) (1999) 1456–1466.
[10] L.P. Moroni, F.P. Glasser, Reactions between cement components and U(VI) oxide, Waste Manag. 15 (3) (1995) 243–254.
[11] P.C. Burns, R.C. Ewing, M.L. Miller, Incorporation mechanisms of actinide elements into the structures of U6+ phases formed during the oxidation of spent nuclear fuel, J. Nucl. Mater. 245 (1) (1997) 1–9.
[12] E.C. Pearcy, et al., Alteration of uraninite from the Nopal I deposit, Peña Blanca District, Chihuahua, Mexico, compared to degradation of spent nuclear fuel in the proposed U.S. high-level nuclear waste repository at Yucca Mountain, Nevada, Appl. Geochem. 9 (6) (1994) 713–732.
[13] P.C. Burns, Y. Li, The structures of becquerelite and Sr-exchanged becquerelite, Am. Mineral. 87 (4) (2002) 550–557.
[14] R.J. Finch, R.C. Ewing, Clarkeite: new chemical and structural data, Am. Mineral. 82 (5–6) (1997) 607–619.
[15] P. Bots, et al., Formation of stable uranium(vi) colloidal nanoparticles in conditions relevant to radioactive waste disposal, Langmuir 30 (48) (2014) 14396–14405.
[16] P.C. Burns, K.M. Deely, S. Skanthakumar, Neptunium incorporation into uranyl compounds that form as alteration products of spent nuclear fuel: implications for geologic repository performance, Radiochim. Acta/Int. J. Chem. aspects Nucl. Sci. Technol. 92 (3/2004) (2004) 151–160.
[17] A.L. Klingensmith, et al., Neptunium incorporation in sodium-substituted metaschoepite, Am. Mineral. 92 (4) (2007) 662–669.
[18] M. Douglas, et al., Neptunium(V) partitioning to uranium(vi) oxide and peroxide solids, Environ. Sci. Technol. 39 (11) (2005) 4117–4124.
[19] C. Cahill, P. Burns, The structure of agrinierite: a Sr-containing uranyl oxide hydrate mineral, Am. Mineral. 85 (9) (2000) 1294–1297.
[20] E.H.P. Cordfunke, B.O. Loopstra, Preparation and properties of the uranates of calcium and strontium, J. Inorg. Nucl. Chem. 29 (1) (1967) 51–57.
[21] H.R. Hoekstra, J.J. Katz, Studies on the alkaline earth diuranates, J. Am. Chem. Soc. 74 (7) (1952) 1683–1690.
[22] W.H. Zachariasen, Crystal chemical studies of the 5F- series of elements.4. The crystal structure of $Ca(UO_2)O_2$ and $Sr(UO_2)O_2$, Acta Crystallogr. 1 (1–6) (1948) 281–285.
[23] B.O. Loopstra, H.M. Rietveld, The structure of some alkaline-earth metal uranates, Acta Crystallogr. Sect. B 25 (4) (1969) 787–791.
[24] H. Rietveld, The crystal structure of some alkaline earth metal uranates of the type M3UO6, Acta Crystallogr. 20 (4) (1966) 508–513.
[25] V.A. Volkovich, et al., Vibrational spectra of alkali metal (Li, Na and K) uranates and consequent assignment of uranate ion site symmetry, Vib. Spectrosc. 17 (1) (1998) 83–91.
[26] V.A. Volkovich, et al., Solubilities and solubilisation enthalpies of alkali metal uranates(VI) in carbonate melts, Phys. Chem. Chem. Phys. 1 (14) (1999) 3297–3302.
[27] V. Volkovich, et al., Oxidation of UO2 in molten alkali-metal carbonate mixtures: Formation of uranates and diuranates, J. Chem. Society-Faraday Trans. 92 (24) (1996) 5059–5065.
[28] D.M. Antonelli, J.Y. Ying, Synthesis of hexagonally packed mesoporous TiO2 by a modified sol–gel method, Angewandte Chemie Int. Ed. Engl. 34 (18) (1995) 2014–2017.
[29] Y. Lu, et al., Modifying the surface properties of superparamagnetic iron oxide nanoparticles through a sol-gel approach, Nano Lett. 2 (3) (2002) 183–186.
[30] A.K. Gupta, M. Gupta, Synthesis and surface engineering of iron oxide nanoparticles for biomedical applications, Biomaterials 26 (18) (2005) 3995–4021.
[31] S. Laurent, et al., Magnetic iron oxide nanoparticles: synthesis, stabilization, vectorization, physicochemical characterizations, and biological applications, Chem. Rev. 108 (6) (2008) 2064–2110.
[32] J. Janov, P.G. Alfredson, V.K. Vilkaitis, The influence of precipitation conditions on the properties of ammonium diuranate and uranium dioxide powders, J. Nucl. Mater. 44 (2) (1972) 161–174.
[33] R.A. Reibold, et al., Synthesis and characterization of a low-density urania (UO3) aerogel, J. Non-Crystalline Solids 319 (3) (2003) 241–246.
[34] A.H. Le Page, A.G. Fane, The kinetics of hydrogen reduction of UO3 and U3O8 derived from ammonium diuranate, J. Inorg. Nucl. Chem. 36 (1) (1974) 87–92.
[35] M.C. Ball, et al., The thermal decomposition of ammonium diuranate, J. Inorg. Nucl. Chem. 36 (7) (1974) 1527–1529.
[36] T.R. Griffiths, V.A. Volkovich, A review of the high temperature oxidation of uranium oxides in molten salts and in the solid state to form alkali metal uranates, and their composition and properties, J. Nucl. Mater. 274 (3) (1999) 229–251.
[37] W. Baxter, Plutonium Finishing and Product Packaging at Thorp, 1989.
[38] J.H. Gladstone, T. Dale, Researches on the refraction, dispersion, and sensitiveness of liquids, Philos. Trans. R. Soc. Lond. 153 (1863) 317–343.
[39] E.S. Larsen, The Microscopic Determination of the Nonopaque Minerals, US Government Printing Office, 1921.
[40] J. Mandarino, The Gladstone-Dale relationship. Part I: derivation of new constants, Can. Mineral. 14 (4) (1976) 498–502.
[41] V. Rogova, et al., Bauranoite and metacalciouranoite, new minerals of the hydrous uranium oxides group, Int. Geol. Rev. 16 (2) (1974) 214–219.
[42] A. Savitzky, M.J.E. Golay, Smoothing and differentiation of data by simplified least squares procedures, Anal. Chem. 36 (8) (1964) 1627–1639.
[43] R. Hill, C. Howard, Quantitative phase analysis from neutron powder diffraction data using the Rietveld method, J. Appl. Crystallogr. 20 (6) (1987) 467–474.
[44] F. Izumi, The Rietveld Method, 1992.
[45] M.D. Abràmoff, P.J. Magalhães, S.J. Ram, Image processing with image, J. Biophot. Int. 11 (7) (2004) 36–42.
[46] D.L. Parkhurst, C. Appelo, User's Guide to PHREEQC (Version 2): a Computer Program for Speciation, Batch-reaction, One-dimensional Transport, and Inverse Geochemical Calculations, 1999.
[47] D.L. Parkhurst, C. Appelo, Description of Input and Examples for PHREEQC Version 3: a Computer Program for Speciation, Batch-reaction, One-dimensional Transport, and Inverse Geochemical Calculations, US Geological Survey, 2013.
[48] E. Giffaut, et al., Andra thermodynamic database for performance assessment: ThermoChimie, Appl. Geochem. 49 (2014) 225–236.
[49] I. Grenthe, H. Wanner, I. Forest, Chemical Thermodynamics of Uranium, 1992.
[50] R. Guillaumont, F.J. Mompean, Update on the Chemical Thermodynamics of Uranium, Neptunium, Plutonium, Americium and Technetium, 2003.
[51] J. Bruno, A. Sandino, The solubility of amorphous and crystalline schoepite in neutral to alkaline aqueous solutions, in: MRS Proceedings, Cambridge Univ Press, 1988.
[52] M. Rodahl, et al., Quartz crystal microbalance setup for frequency and Q-factor measurements in gaseous and liquid environments, Rev. Sci. Instrum. 66 (7) (1995) 3924–3930.
[53] G. Sauerbrey, Verwendung von Schwingquarzen zur Wägung dünner Schichten und zur Mikrowägung, Z. für Phys. 155 (2) (1959) 206–222.
[54] G. Sauerbrey, The Use of Quartz Crystal Oscillators for Weighing Thin Layers and for Microweighing Applications, 1991.
[55] R. Vochten, L. Van Haverbeke, R. Sobry, Transformation of schoepite into uranyl oxide hydrates of the bivalent cations Mg 2+, Mn 2+ and Ni 2+, J. Mater. Chem. 1 (4) (1991) 637–642.
[56] G. Meinrath, Uranium (VI) speciation by spectroscopy, J. Radioanal.cal Nucl. Chem. 224 (1–2) (1997) 119–126.
[57] J. Skakle, L. Moroni, F. Glasser, X-ray diffraction data for two new calcium uranium (VI) hydrates, Powder Diffr. 12 (02) (1997) 81–86.
[58] F. Zhang, et al., Structural transitions and electron transfer in coffinite, USiO4, at high pressure, Am. Mineral. 94 (7) (2009) 916–920.
[59] M. Burdick, H. Parker, Effect of particle size on bulk density and strength properties of uranium dioxide specimens, J. Am. Ceram. Soc. 39 (5) (1956) 181–187.
[60] F. Quilès, A. Burneau, Infrared and Raman spectra of uranyl(VI) oxo-hydroxo complexes in acid aqueous solutions: a chemometric study, Vib. Spectrosc. 23 (2) (2000) 231–241.
[61] F. Quilès, et al., Hydrolysis of uranyl(vi) in acidic and basic aqueous solutions using a noncomplexing organic base: a multivariate spectroscopic and statistical study, Inorg. Chem. 50 (7) (2011) 2811–2823.
[62] D. Palmer, C. Nguyen-Trung, Aqueous uranyl complexes. 3. Potentiometric measurements of the hydrolysis of uranyl(VI) ion at 25°C, J. Solut. Chem. 24 (12) (1995) 1281–1291.
[63] A. Froideval, et al., pH dependence of uranyl retention in a quartz/solution

system: an XPS study, J. Colloid Interface Sci. 266 (2) (2003) 221–235.
[64] E.R. Sylwester, E.A. Hudson, P.G. Allen, The structure of uranium (VI) sorption complexes on silica, alumina, and montmorillonite, Geochim. Cosmochim. Acta 64 (14) (2000) 2431–2438.
[65] R. Demichelis, et al., Stable prenucleation mineral clusters are liquid-like ionic polymers, Nat. Commun. 2 (2011) 590.
[66] G.J.D.A.A. Soler-Illia, et al., Synthesis of metal oxide particles from aqueous media: the homogeneous alkalinization method, J. Dispers. Sci. Technol. 19 (2–7) (1998) 207–228.
[67] R. Van Santen, The Ostwald step rule, J. Phys. Chem. 88 (24) (1984) 5768–5769.
[68] J.-H. Jang, B.A. Dempsey, W.D. Burgos, Solubility of schoepite: comparison and selection of complexation constants for U(VI), Water Res. 40 (14) (2006) 2738–2746.
[69] P. Díaz Arocas, B. Grambow, Solid-liquid phase equilibria of U(VI) in NaCl solutions, Geochim. Cosmochim. Acta 62 (2) (1998) 245–263.
[70] R. Vochten, L. Vanhaverbeke, Transformation of schoepite into the uranyl oxide hydrates - becquerelite, billietite and wolsendorfite, Mineral. Petrol. 43 (1) (1990) 65–72.
[71] R. Vochten, E. Degrave, H. Lauwers, Transformation of synthetic U3o8 into different uranium oxide hydrates, Mineral. Petrol. 41 (2–4) (1990) 247–255.
[72] N.G. Chernorukov, O.V. Nipruk, E.L. Kostrova, Synthesis and study of sodium uranate Na2U2O7·6H2O and of products of its dehydration and thermal decomposition, Radiochemistry 58 (2) (2016) 124–127.
[73] J. Cejka, Infrared spectroscopy and thermal analysis of the uranyl minerals, Rev. Mineral. Geochem. 38 (1) (1999) 521–622.
[74] V. Baran, M. Tympl, Uranates as a form of uranyl hydrolytic complexes, J. Inorg. Nucl. Chem. 28 (1) (1966) 89–98.
[75] M. Harju, et al., Water adsorption on plasma sprayed transition metal oxides, Appl. Surf. Sci. 249 (1–4) (2005) 115–126.
[76] S.K. Sali, S. Sampath, V. Venugopal, Thermal studies on alkaline earth uranates, J. Nucl. Mater. 277 (1) (2000) 106–112.